Available online at www.sciencedirect.com
ScienceDirect
Advances in Space Research 46 (2010) 974–983
ADVANCES IN SPACE RESEARCH (a COSPAR publication)
www.elsevier.com/locate/asr

# Comparing topside and bottomside-measured characteristics of the F2 layer peak

Patrick A. Nsumei [a], Bodo W. Reinisch [a,*], Xueqin Huang [a], Dieter Bilitza [b]

[a] Center for Atmospheric Research, University of Massachusetts Lowell, 600 Suffolk Street, Lowell, MA 01854, USA
[b] Space Weather Laboratory, George Mason University, Fairfax, VA 22030, USA

Received 22 February 2010; received in revised form 11 June 2010; accepted 14 June 2010

**Abstract**

The ionospheric characteristics of the F2 layer peak have been measured with ionosondes from the ground or with satellites from space. The most common characteristics are the F2-peak density *NmF*2 and peak height *hmF*2. In addition to these two parameters this paper studies the F2-peak scale height. Comparing the median values of *hmF*2 and *NmF*2 obtained from topside and bottomside sounding shows good agreement in general. The Chapman scale height values for the F2 layer peak derived from topside profiles, $H_{m,top}$, are generally several times larger than $H_{m,bot}$ derived from bottomside profiles.


*Keywords:* F2 layer profiles; Vary–Chap profile; Scale height; Digisonde; ISIS-2

## 1. Introduction

In the study of the electron density distribution in the ionosphere in connection with radio communication and positioning applications, information about the F2 layer peak characteristics is by far the most important input. The key characteristics of the F2 layer peak, namely the peak height *hmF*2, the peak electron density *NmF*2, and the Chapman scale height *H*, play crucial roles in ionospheric dynamics and are routinely measured along with the electron density ($N_e$) profiles by the Global Ionospheric Radio Observatory (GIRO) using the ground-based Digisonde network (Reinisch et al., 2009). It is important to note that *H* used here is the scale height for the general Chapman function that is deduced for a multi-constituent gas (Rishbeth and Garriott, 1969) (see Section 3) and involves a scale height that is continuously varying with height. This is different from the simplified Chapman function which uses a constant scale height for the whole topside F2 layer that is deduced for a single-constituent (O) gas and constant thermospheric temperature.

A large database of bottomside-measured data is available at http://ulcar.uml.edu/GIRO/ (Galkin et al., 2006). In this paper, we compare the peak characteristics obtained from bottomside sounding at a few selected stations with those obtained from topside sounding measurements (e.g., Kutiev et al., 2006; Kutiev and Marinov, 2007; Depuev and Pulinets, 2004).

Topside $N_e$ profile data are not as abundant as the bottomside data because only a few satellite missions, for example Alouette, ISIS-1 and ISIS-2 (Benson and Bilitza, 2009), have been dedicated to routine $N_e$ profile measurements. These topside measurements were made in the 1970s, while GIRO profile data are routinely available only for the last three decades. We therefore had to contend ourselves with comparing monthly median values rather than doing case-by-case comparisons. This process should be adequate, however, for revealing the presence of any systematic differences or biases. Because of the limited signal-to-noise ratio in the topside ionograms near the F2 layer critical frequency foF2 there is concern that the

* Corresponding author.
*E-mail addresses:* Patrick_Nsumei@uml.edu (P.A. Nsumei), Bodo_Reinisch@uml.edu (B.W. Reinisch), Xueqin_Huang@uml.edu (X. Huang), dbilitza@gmu.edu (D. Bilitza).

0273-1177/$36.00 © 2010 COSPAR. Published by Elsevier Ltd. All rights reserved.
doi:10.1016/j.asr.2010.06.027

extracted foF2 values may be too small, and that as a consequence the calculated profiles will not reach down to the actual F2-peak height. To address this concern about the topside measurements, we compared the F2-peak characteristics measured by topside sounding with those measured at a number of ionosonde stations.

In the second part of this study, we discuss the calculation of the Vary–Chap scale height function $H(h)$ and the scale height value $H_m$ at the F2 layer peak (Ram et al., 2009; Zhang et al., 2006; Reinisch et al., 2007), derived from bottomside and topside $N_e$ profiles. For selected locations, the $H_m$ values derived from ground-based measurements, $H_{m,bot}$, are then compared with the corresponding $H_{m,top}$, values determined from topside $N_e$ profiles. The diurnal and latitudinal variations of the ratio $H_{m,top}/H_{m,bot}$ are presented for a number of locations. We show in Section 4 that this ratio can vary from 0.5 to ~4 with local time and latitude.

## 2. Data and observations

This study uses two datasets: (1) ground-based digisonde measured peak characteristics from Ebro Observatory, Spain (MLAT 43°) with data covering the period of 1988–2001, Boulder, USA (MLAT 48°) for the period of 2004–2008, and Millstone Hill, USA (MLAT 53°) for the period 1992–2008 data; and (2) ISIS-2 topside $N_e$ measurements covering the period of 1973–1983. The ISIS-2 latitudinal data coverage is such that there are fewer $N_e$ data at lower latitudes than at higher latitudes, and for the topside/bottomside comparison of *hmF*2 and *NmF*2 we selected the three locations mentioned above as a compromise approach. Our analysis includes all available data for which F10.7 < 120 and Kp < 3. The data are first grouped according to season, magnetic latitude (MLAT), and magnetic local time (MLT). Data from two additional ionosonde sites, Ramey (MLAT 28.5°) and Jicamarca (MLAT −1.4°), were used for the $H_m$ comparison (Section 3).

### 2.1. NmF2 and hmF2 at Roquetes (Ebro), Spain

Fig. 1 shows the median values of *hmF*2 and *NmF*2 for different seasons, obtained from bottomside and topside sounding measurements, together with the IRI model values (Bilitza, 2001, 2004; Bilitza et al, 2006). The topside data displayed in Fig. 1 cover the magnetic latitude range from 40° to 46° and include all longitudes. In general, the topside and bottomside values are in fair agreement showing no significant systematic differences except for the spring evening period. Here, the topside *hmF*2 values exceed the bottomside values by up to 110 km (Fig. 1b), while the topside *NmF*2 values are up to a factor of 2 smaller than the bottomside values (Fig. 1f). This pattern could be caused by a larger number of topside ionograms during that period that are incorrectly scaled. When the TOPIST autoscaling determines an foF2 value smaller than the actual value, the profile calculation will automatically derive a larger *hmF*2 value. The reason that this effect is only seen during spring may be the relative scarcity of topside profiles during this period resulting in a small data sample. A similar behavior, although to a smaller degree, is seen in winter between 18 and 21 MLT. During afternoon hours in winter the topside *NmF*2 is also too low and in this case *hmF*2 is not affected. This feature is not understood.

For a quantitative analysis we investigated the ratios

$$D_{\mathrm{hm}} = \frac{hmF2(\mathrm{topside}) - hmF2(\mathrm{bottomside})}{hmF2(\mathrm{bottomside})} \tag{1a}$$

and

$$D_{\mathrm{Nm}} = \frac{NmF2(\mathrm{topside}) - NmF2(\mathrm{bottomside})}{NmF2(\mathrm{bottomside})} \tag{1b}$$

The bar graphs in Fig. 2 represent the percentage deviations for $D_{\mathrm{hm}}$ and $D_{\mathrm{Nm}}$ showing that 89% of the topside and bottomside median *hmF*2 data deviate by less than 15%, and 75% of the topside and bottomside median *NmF*2 data deviate by less than 30%. In general, Fig. 2a and b shows that over 70% of the median values of the peak characteristics from topside measurements are in good agreement with the bottomside values.

### 2.2. NmF2 and hmF2 at Boulder, USA

Fig. 3 shows the median *hmF*2 and *NmF*2 values and the IRI model values for Boulder, CO for different seasons. The topside data used in Fig. 3 cover the MLAT range of 46–50° and include all longitudes. Again, we see that the peak characteristics measured from the topside follow very similar trends as those measured from the bottomside and the IRI model.

The bar graph in Fig. 4a shows that for Boulder over 90% of the topside median *hmF*2 data fall within deviations of $D_{\mathrm{hm}} = \pm 15\%$, and Fig. 4b shows that about 70% of the topside median *NmF*2 data fall within deviations of $D_{\mathrm{Nm}} = \pm 30\%$. This implies a fairly good agreement between the median values of the peak characteristics measured from the topside and bottomside. Detailed inspection revealed that the agreement is best for regions where sufficient topside data are available (not shown here).

### 2.3. NmF2 and hmF2 at Millstone Hill

Fig. 5 shows the medians of measured bottomside and topside *hmF*2 and *NmF*2 values, and the IRI model predictions over Millstone for different seasons. The topside data used in Fig. 5 cover the MLAT range of 50–56° over all longitudes.

For Millstone Hill, over 80% of the topside median *hmF*2 data fall within deviations of $D_{\mathrm{hm}} = \pm 15\%$ (Fig. 6a), however, less than 50% of the topside median *NmF*2 data fall within deviations of $D_{\mathrm{Nm}} = \pm 30\%$. This shows a fairly good agreement between the topside-measured and bottomside-measured *hmF*2 values, the *NmF*2

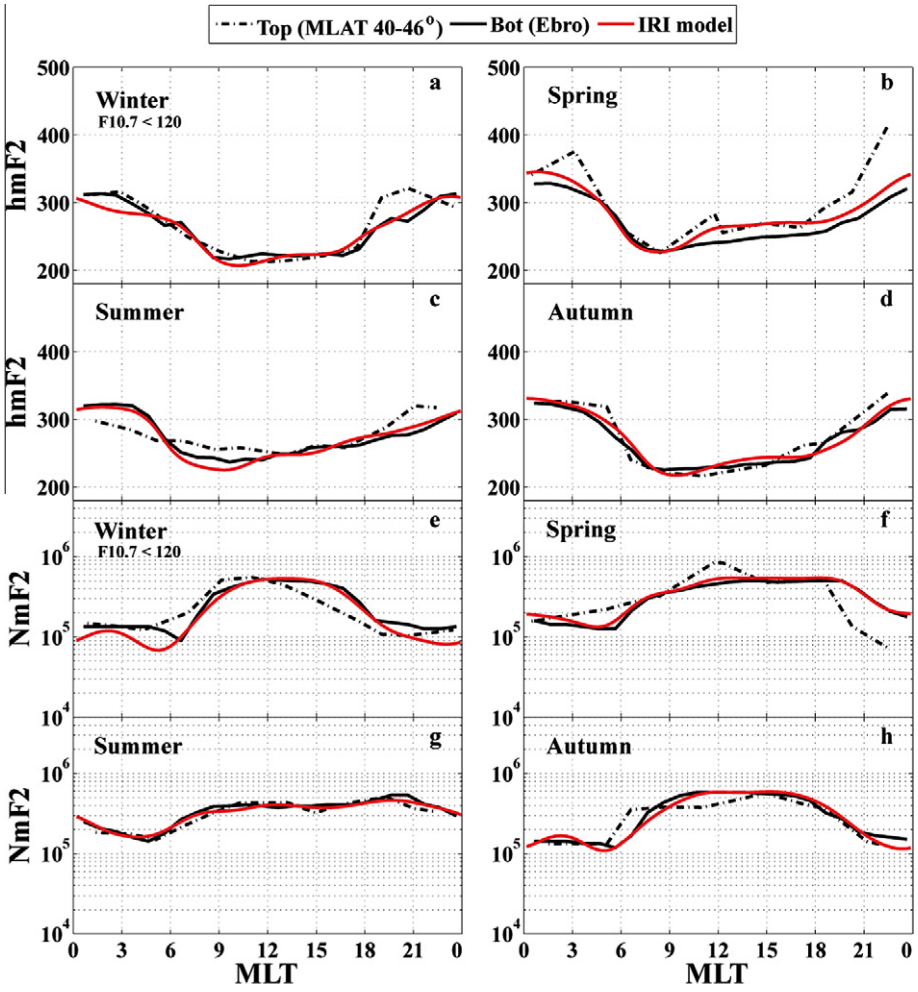


Fig. 1. F2 layer peak characteristics at Ebro (MLAT 43°) measured from the topside and bottomside, and the IRI model values during periods of low F107 index (F107 < 120) and low magnetic activity (Kp < 3). Figure panel (a) *hmF*2–winter, (b) *hmF*2–spring, (c) *hmF*2–summer, (d) *hmF*2–autumn, (e) *NmF*2–winter, (f) *NmF*2–spring, (g) *NmF*2–summer, and (h) *NmF*2–autumn.

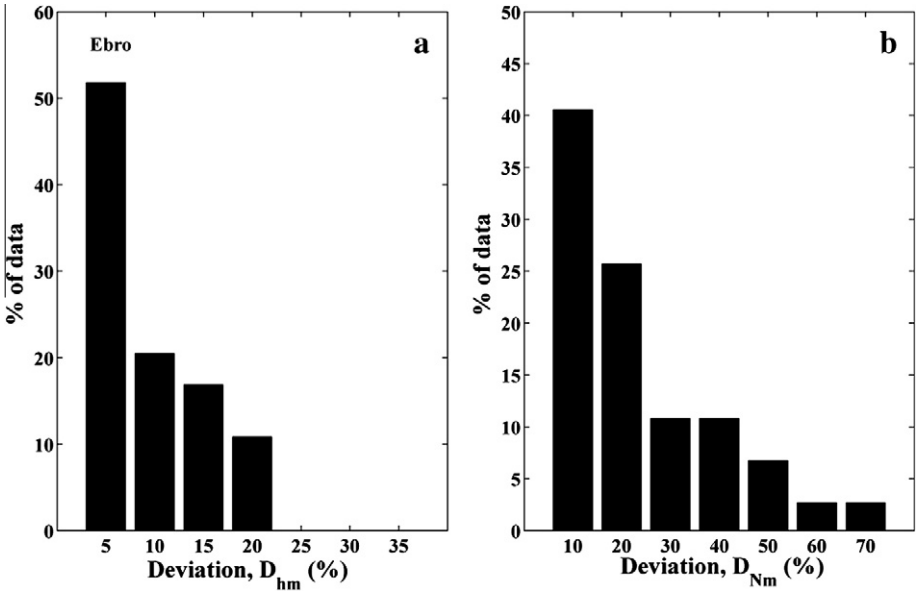


Fig. 2. Bar chart representations of the deviations in F2-peak characteristics over Ebro, Spain, bar graphs of % of median data vs. $D_{hm}$ (a), and vs. $D_{Nm}$ (b).

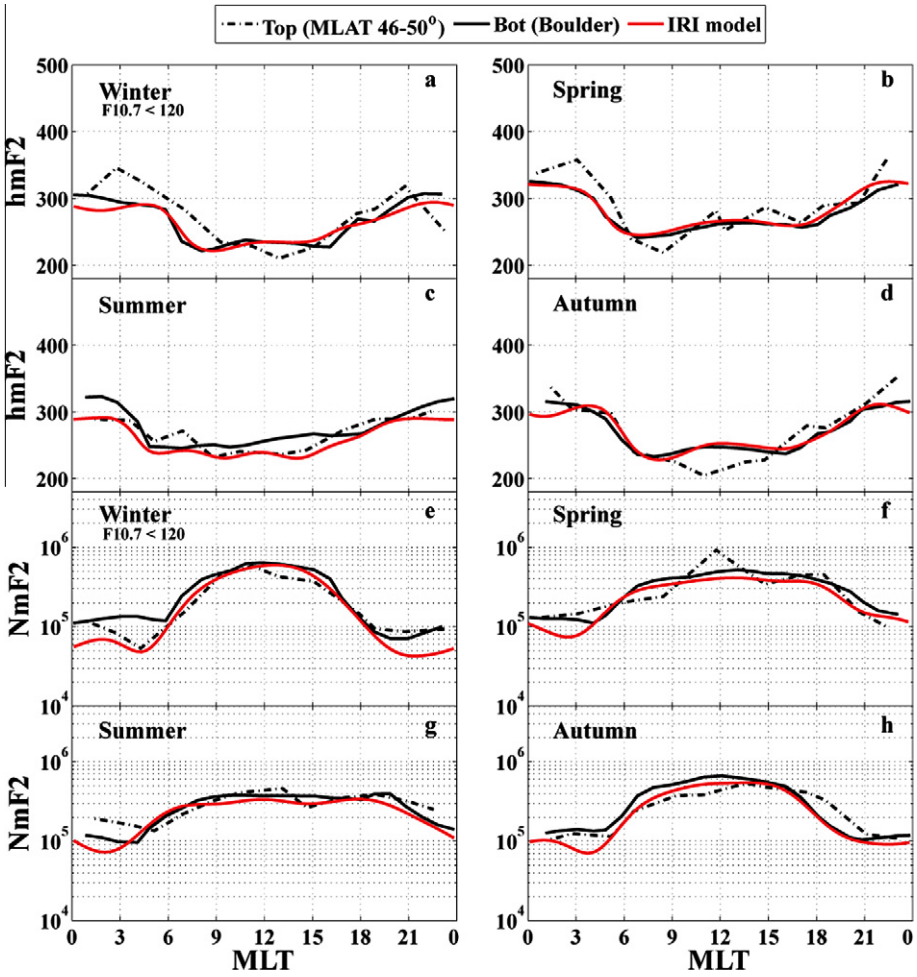


Fig. 3. Diurnal variations of F2-peak characteristics at Boulder (MLAT 48°) measured from the topside and bottomside, and IRI model values during periods of low F107 index (F107 < 120) and low magnetic activity (Kp < 3). Figure panel (a) *hmF2*/winter, (b) *hmF2*/spring, (c) *hmF2*/summer, (d) *hmF2*/autumn, (e) *NmF2*/winter, (f) *NmF2*/spring, (g) *NmF2*/summer, and (h) *NmF2*/autumn.

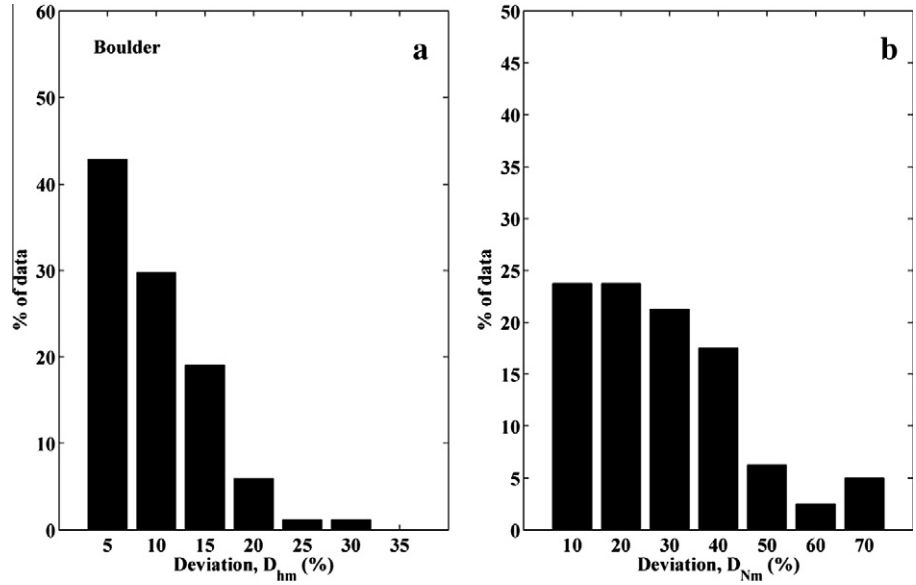


Fig. 4. Bar chart of deviations in peak characteristics over Boulder, Colorado: bar graphs of % of median data vs. $D_{hm}$ (a), and vs. $D_{Nm}$ (b).

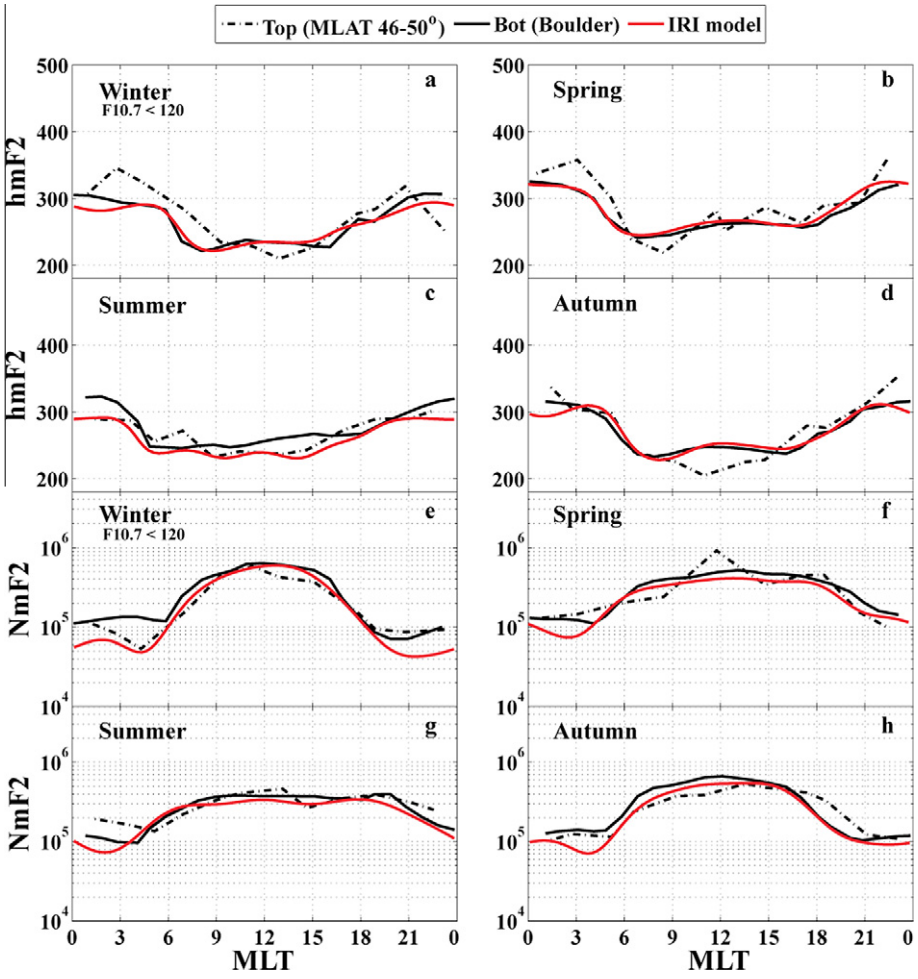


Fig. 5. Diurnal variations of F2-peak characteristics at Millstone Hill (MLAT 53°) measured from the topside and bottomside, and IRI model peak characteristics during periods of low F107 index (F107 < 120) and low geomagnetic activity (Kp < 3). Figure panel (a) *hmF*2/winter, (b) *hmF*2/spring, (c) *hmF*2/summer, (d) *hmF*2/autumn, (e) *NmF*2/winter, (f) *NmF*2/spring, (g) *NmF*/summer, and (h) *NmF*2/autumn.

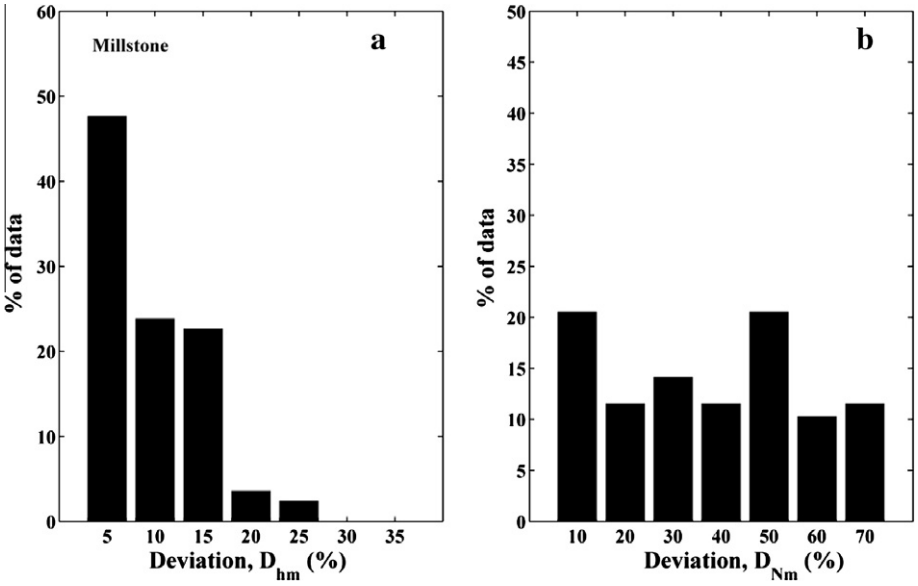


Fig. 6. Bar chart representations of the deviations in peak characteristics over Millstone Hill: bar graph of % of median data vs. $D_{hm}$ (a), and vs. $D_{Nm}$ (b).

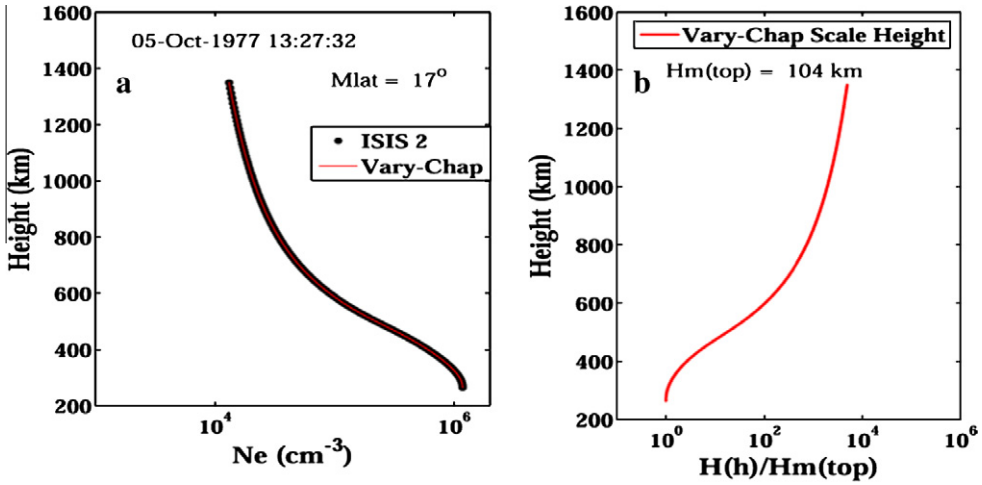


Fig. 7. Left: ISIS-2 $N_e$ profile (black dots), right: calculated scale height $H(h)/H_m$ profile from the $N(h)$ profile shown on the left. The Vary–Chap profile (red line) calculated with $H(h)$ shown on the right is superimposed on the measured profile on the left. (For interpretation of color mentioned in this figure the reader is referred to the web version of the article.)

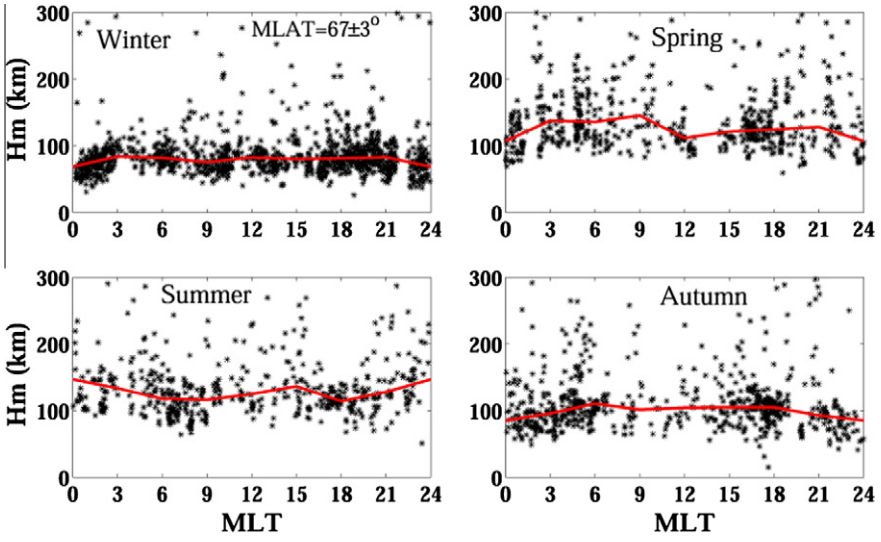


Fig. 8. Seasonal plot of topside $H_m$ vs. MLT for MLAT = 67 ± 3°. Top left (winter), top right (spring), bottom left (summer) and bottom right (autumn). The red line represents the median values. (For interpretation of color mentioned in this figure the reader is referred to the web version of the article.)

agreement, however, is marginal. The larger ionospheric variability at high magnetic latitudes (MLAT at Millstone Hill is 53°) is most likely the reason for the lower agreement of the topside and bottom values at Millstone compared to the stations at lower latitude, Ebro and Boulder.

## 3. Vary–Chap representation of $N_e$ profiles and calculation of the Vary–Chap scale height function H(h)

The general α-Chapman profile given by Rishbeth and Garriott (1969) has a neutral scale height $H(h)$ that varies with height, and we therefore call it the Vary–Chap function (Reinisch et al. 2007):

$$N_e = N_m \left(\frac{H_m}{H(h)}\right)^{1/2} \exp\left[\frac{1}{2}(1 - y - \exp(-y))\right] \tag{2a}$$

$$\text{with} \quad y = \int_{h_m}^{h} \frac{dh}{H(h)} \tag{2b}$$

Representation of a measured $N(h)$ profile as a Vary–Chap function requires knowledge of $H(h)$. Huang and Reinisch (2001) have shown that Eq. (1a) can be solved for $H(h)$ as function of $N(h)$:

$$H(h) = H_m \left(\frac{N(h)}{N_m}\right)^{-2} X(h)[1 - \ln X(h)] \tag{3a}$$

$$\text{with} \quad X(h) = 1 + \frac{1}{H_m} \int_{h_m}^{h} \left(\frac{N(h)}{N_m}\right)^{2} dh \tag{3b}$$

Physically reasonable $H(h)$ functions are obtained for any value $H_m$ that satisfies the condition

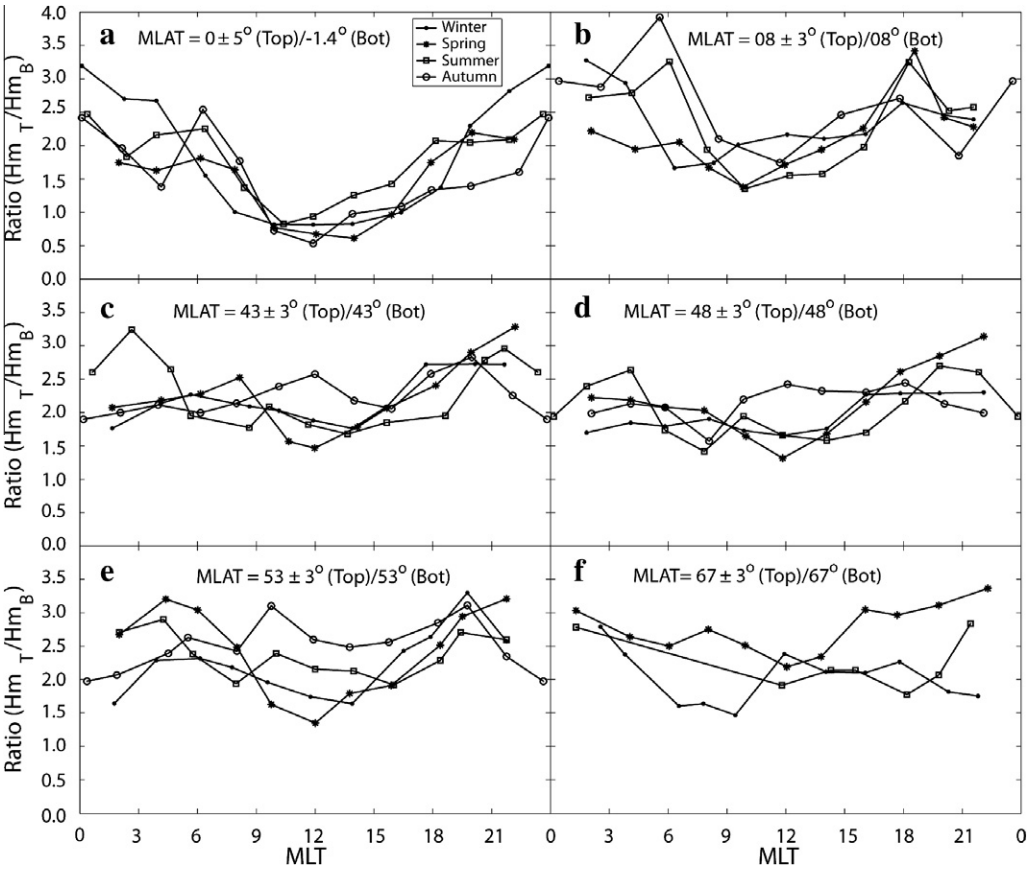


Fig. 9. Median $H_{m,top}$ vs. MLT for (a) MLAT = 0 ± 5°, (b) MLAT = 08 ± 3°, (c) MLAT = 48 ± 3°, (d) MLAT = 53 ± 3°, (e) MLAT = 67 ± 3°, and (f) MLAT = 87 ± 3°.

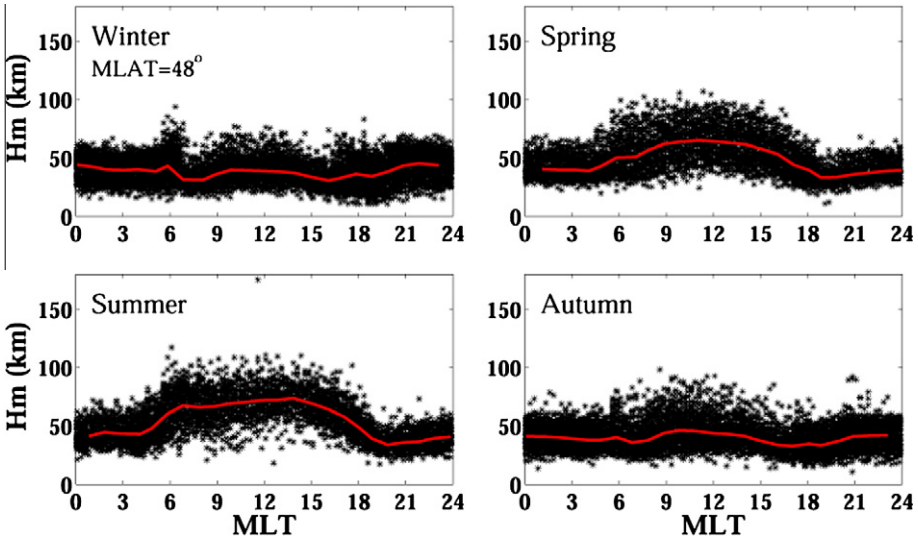


Fig. 10. Diurnal and seasonal variations of $H_{m,bot}$ for Millstone Hill (MLAT = 53°). The red line represents the median values. (For interpretation of color mentioned in this figure the reader is referred to the web version of the article.)

$$H_m > 0.6 \int_{h_m}^{h_s} \left(\frac{N(h)}{N_m}\right)^2 dh \quad (3c)$$

for the topside profile, where $h_s$ is the height of the satellite, and

$$H_m \geqslant \int_{h_0}^{h_m} \left(\frac{N(h)}{N_m}\right)^2 dh \quad (3d)$$

for the bottomside profile (Reinisch and Huang, 2004) where $h_0$ is the bottom height of the F2 layer. Fig. 7

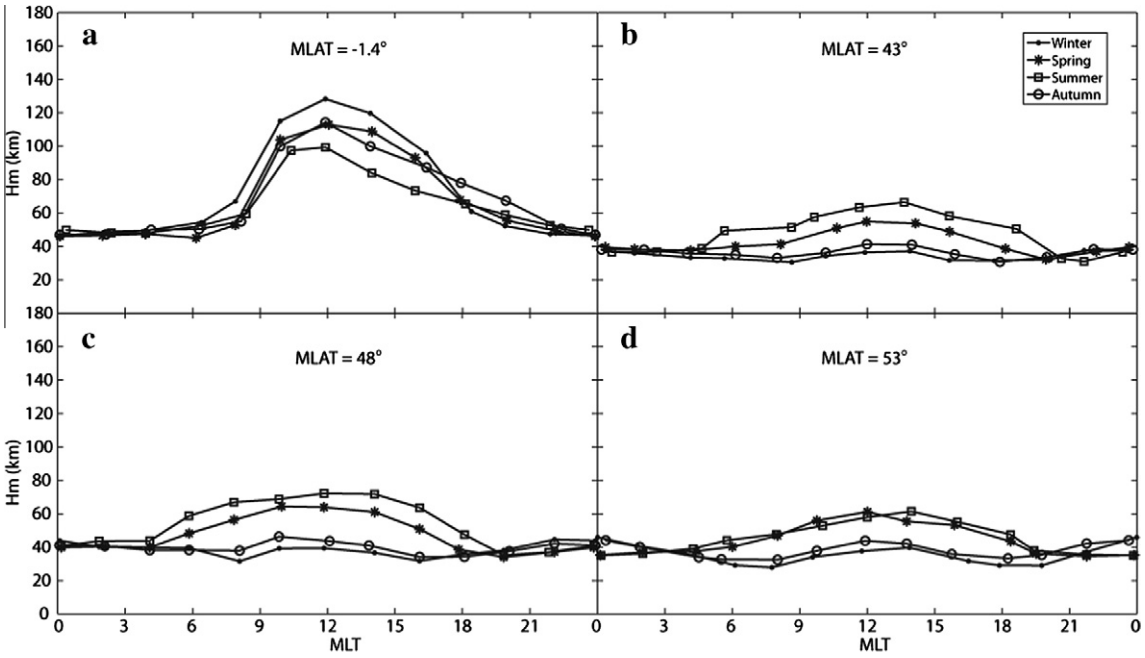


Fig. 11. Diurnal and seasonal variations of $H_{m,bot}$ at four locations (a) Jicamarca, (b) Ebro, (c) Boulder, and (d) Millstone.

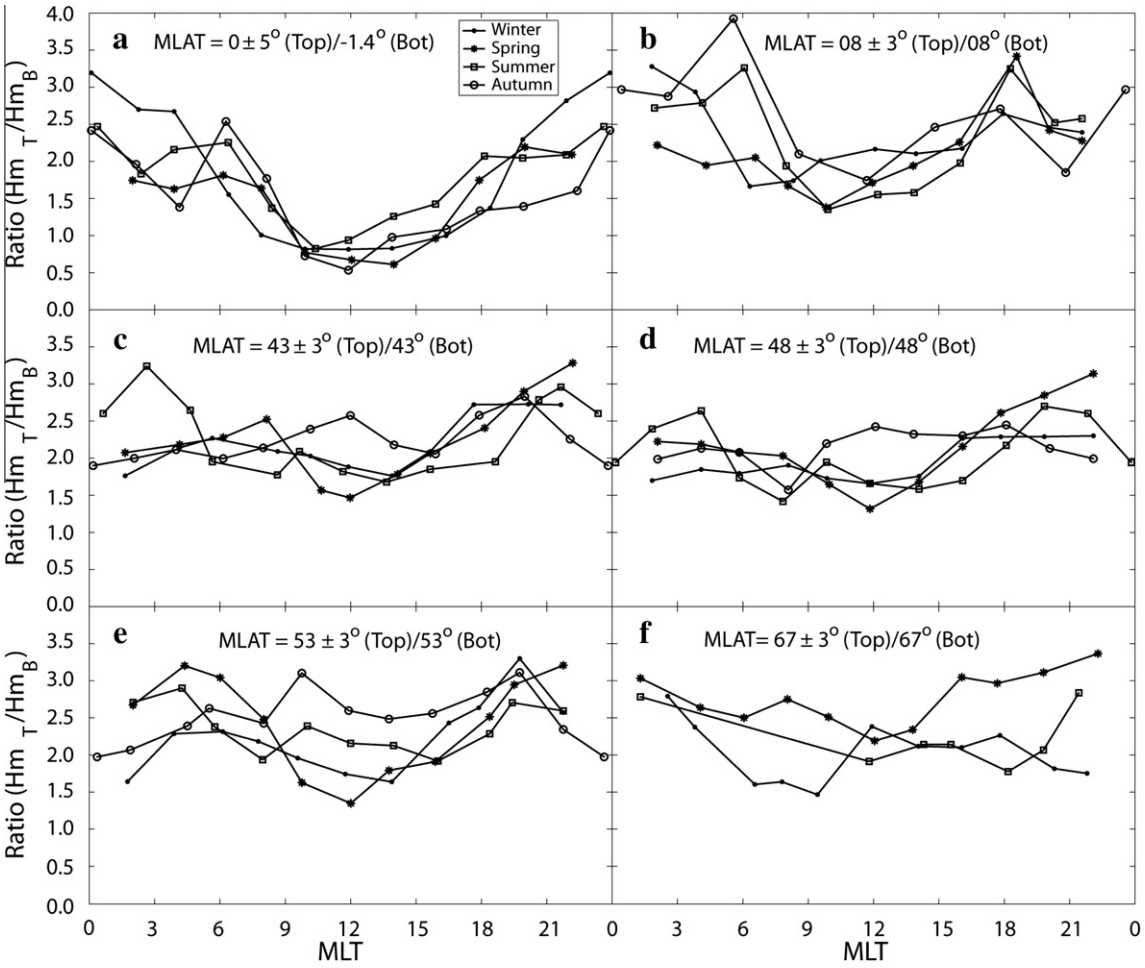


Fig. 12. Seasonal plot of $R_{\mathrm{Hm}}$ (ratio of topside to bottomside-measured $H_m$) vs. MLT for (a) MLAT $= 0 \pm 5°$ (topside) and $-1.4°$ (bottomside), (b) MLAT $= 08 \pm 3°$ (topside) and 08° (bottomside), (c) MLAT $= 43 \pm 3°$ (topside) and 43° (bottomside), (d) MLAT $= 48 \pm 3°$ (topside) and 48° (bottomside), (e) MLAT $= 53 \pm 3°$ (topside) and 53° (bottomside) and (f) MLAT $= 67 \pm 3°$ (topside) and 67° (bottomside).

illustrates the duality relation of $N(h)$ and $H(h)$. The left panel shows a measured topside profile (black dots), and the right panel the derived $H(h)$ function. Of course, by inserting the derived $H(h)$ function into Eq. (3a), the measured $N(h)$ function is reproduced (red curve in left panel).

For our analysis we have arbitrarily set $H_{m,bot}$ and $H_{m,top}$ equal to $H_m = \int (N_e/\boldsymbol{Nm})^2 dh$ at the bottomside or topside, respectively, satisfying Eqs. (3c) and (3d). One would therefore expect $H_{m,top} > H_{m,bot}$ since the topside electron content is generally larger than the bottomside content, and this was indeed reported by Kutiev et al. (2009).

### 3.1. Deriving $H_m$ from topside and bottomside profiles

Fig. 8 shows the diurnal variations of $H_{m,top}$ for different seasons calculated from ISIS-2 $N_e$ profiles using Eq. (3c). This example is for the latitude range of $67 \pm 3°$ where sufficient data were available for most parts of the day. The median values of $H_{m,top}$, connected by a red line, show little diurnal variations at this latitude, and only a small seasonal variations with slightly larger values in spring and summer. The latitudinal variation, illustrated by the six panels in Fig. 9, is also small, and seems to be largest in the equatorial region with a minimum at local noon.

For the $H_{m,bot}$ values more significant diurnal and latitudinal variations have previously been reported (e.g., Nambala et al., 2008; Reinisch et al., 2007). Fig. 10 shows for the mid latitude station Boulder, CO (MLAT = 48°) a clear maximum for $H_{m,bot}$ at local noon during spring and summer. A very large noon maximum is observed at Jicamarca, Peru (MLAT = −1.4°) as shown in panel (a) of Fig. 11. For spring and summer, a noon maximum is also observed at the other three latitudes shown in Fig. 11, Ebro (43°), Boulder (48°), and Millstone (53°).

### 3.2. Comparison of topside and bottomside-measured $H_m$

The discussion in Section 3.1 revealed different diurnal and latitudinal variations of $H_{m,top}$ and $H_{m,bot}$. To asses these differences, we define the ratio $R_{\mathrm{Hm}} = H_{m,top}/H_{m,bot}$ as the ratio of topside-measured $H_m$ to bottomside $H_m$. Fig. 12a–f shows $R_{\mathrm{Hm}}$ vs. MLT for different seasons and latitudes. As expected the topside values of $H_m$ are generally larger than the bottomside values, an exception is seen over the magnetic equator at noon. The $R_{\mathrm{Hm}}$ values range from 0.5 to 4; the lowest values of $R_{\mathrm{Hm}}$ occur around noon.

## 4. Summary

We have presented data of the F2-peak characteristics *hmF*2, *NmF*2, and $H_m$ measured by ionosondes from above or below the F2 layer peak. We used ISIS-2 topside profiles from the 1970s and bottomside profiles measured at five digisonde stations during more recent times, limiting the analysis to comparing monthly median values. Our study shows that in regions where sufficient topside-measured peak data were available, the peak heights show good agreement with those measured at three ground stations, and both are well represented by the IRI-2001 model. For *NmF*2, good agreement between topside-measured and bottomside-measured values is found at two stations, Ebro and Boulder, while significant discrepancies seem to exist for Millstone Hill. This station is at fairly high magnetic latitude (53° MLAT) compared to Ebro and Boulder, and the increased ionospheric variability is very likely the cause for the discrepancies. Furthermore, the data we compared were not based on simultaneous measurements and some of the differences could be due to the longitudinal and/or solar cycle biases of either one of the two data sets (more likely the satellite data set). It is also important to remember that the topside data used in this study covered a certain range of magnetic latitudes and included all longitudes. Therefore, some of the observed discrepancies may be the result of the type of binning used. In summary, we conclude that topside sounding data provide valid measurements of *hmF*2 and *NmF*2.

The $H_m$ values derived from topside and bottomside sounding are different physical quantities representing the integral of the squared normalized electron density of the topside and bottomside profile. Since the topside electron content is usually larger than the bottomside content, $H_{m,top}$ is mostly larger than $H_{m,bot}$. *Our analysis indicates that* $H_{m,top}$ shows little diurnal and latitudinal variation. Since $H_m = \int (N_e/Nm)^2 dh$ , this result means that the normalized topside content stays constant with time and latitude. This is not the case for the normalized bottomside content, however.

## Acknowledgment

This research was supported by NASA Grant NNX09AJ74G and by the AF Research Laboratory under contract FA8718-06-C-0072.

## References

Benson, R.F., Bilitza, D. New satellite mission with old data: Rescuing a unique data set. Radio Sci. 44, RS0A04, doi:10.1029/2008RS004036, 2009.

Bilitza, D. International reference ionosphere 2000. Radio Sci. 36 (2), 261–275, 2001.

Bilitza, D. A correction for the IRI topside electron density model based on Alouette/ISIS topside sounder data. Adv. Space. Res. 33 (#6), 838–843, 2004.

Bilitza, D., Reinisch, B.W., Radicella, S.M., Pulinets, S., Gulyaeva, T., Triskova, L. Improvements of the international reference ionosphere model for the topside electron density profile. Radio Sci. 41, RS5S15, doi:10.1029/2005RS003370, 2006.

Depuev, V.H., Pulinets, S.A. A global empirical model of the ionospheric topside electron density. Adv. Space Res. 34, 2016–2020, 2004.

Galkin, I.A., Khmyrov, G.M., Kozlov, A., Reinisch, B.W., Huang, X., Kitrosser, D.F. Ionosonde networking, databasing, and web serving. Radio Sci. 41 (5), RS5S33, doi:10.1029/2005RS003384, 2006.

Huang, X., Reinisch, B.W. Vertical total electron content from ionograms in real time. Radio Sci. 36, 335–342, 2001.

Kutiev, I.S., Marinov, P.G., Watanabe, S. Model of topside ionosphere scale height based on topside sounder data. Adv. Space Res. 37, 943–950, 2006.

Kutiev, I., Marinov, P. Topside sounder model of scale height and transition height characteristics of the ionosphere. Adv. Space Res. 39, 759–766, 2007.

Kutiev, I., Marinov, P., Belehaki, A., Reinisch, B., Jakowski, N. Reconstruction of topside density profile by using the topside sounder model profiler and digisonde data. Adv. Space Res. 43, 1683–1687, 2009.

Nambala, Fred-Joe, Lee-Anne, McKinnell, Elijah, Oyeyemi Variations in the ionospheric scale height parameter at the F2 peak over Grahamstown, South Africa. Adv. Space Res. 42, 707–711, 2008.

Ram, S., Tulasi, S.-Y., Su, C., Liu, H., Reinisch, B.W., McKinnell, L.-A. Topside ionospheric effective scale heights (HT) derived with ROCSAT-1 and ground-based ionosonde observations at equatorial and mid-latitude stations. J. Geophys. Res. 114, A10309, doi:10.1029/2009JA014485, 2009.

Reinisch, B.W., Huang, X. Deducing topside profiles and total electron content from bottomside ionograms. Adv. Space Res. 27 (1), 23–30, 2004.

Reinisch, B.W., Nsumei, P., Huang, X., Bilitza, D.K. Modeling the F2 topside and plasmasphere for IRI using IMAGE/RPI, and ISIS data. Adv. Space Res. 39, 731–738, 2007.

Reinisch, B.W., Galkin, I.A., Khmyrov, G.M., Kozlov, A.V., Bibl, K., Lisysyan, I.A., Cheney, G.P., Huang, X., Kitrosser, D.F., Paznukhov, V.V., Luo, Y., Jones, W., Stelmash, S., Hamel, R., Grochmal, J. The new digisonde for research and monitoring applications. Radio Sci. 44, RS0A24, doi:10.1029/2008RS004115, 2009.

Rishbeth, H., Garriott, O.K. Introduction to Ionospheric Physics. Academic Press, New York, 1969.

Zhang, M.-L., Reinisch, B.W., Shi, S., Wu, Wang, X. Diurnal and seasonal variation of the ionogram-derived scale height at the F2 peak. Adv. Space Res. 37, 967–971, doi:10.1016/j.asr.2006.02.004, 2006.